Fuel Fabrication & Material Innovation

Lightbridge Fuel Fabrication Modeling in ABAQUS with Experimental Comparisons

Kyle M. Paaren[1], Eric Shaber[1], Scott Holcombe[1]

[1]Lightbridge Corporation, Reston, VA

ABSTRACT

Lightbridge Fuel™ is an advanced metallic, nuclear fuel designed for use in existing and future water-cooled reactors. Unique to Lightbridge Fuel, the fabrication process utilizes a forward co-extrusion process to turn cast billets into fuel rods. The design of the billets, extrusion dies, and extrusion parameters allow for material flow to create desired grain structures, fuel and cladding thicknesses, and a metallurgical bond between the fuel and the cladding. To complement and accelerate the Lightbridge Fuel fabrication process, modeling efforts have been performed using ABAQUS Explicit to predict formation of the co-extruded rods, including material final dimension, stresses, and strains. The results from the ABAQUS simulations were compared to destructive testing performed at Idaho National Laboratory, including fuel and cladding thickness, and overall length of each billet. These comparisons will further help benchmark the fabrication parameters, physics, and boundary conditions used within the ABAQUS simulations and allow variations of the co-extrusion process to be modeled for the Lightbridge fuel fabrication qualification program. The results from the ABAQUS simulations provide early insights into fuel mechanical performance, anticipated impacts to the fuel fabrication process, and parameters included in Lightbridge's fuel qualification program.

Keywords: ABAQUS, Modeling, Extrusion, Fuel Fabrication

1.   INTRODUCTION

Lightbridge Corporation has developed preliminary fuel fabrication plans [1], [2], which are being further developed and demonstrated in fabrication facilities at Idaho National Laboratory (INL) as part of Lightbridge's long-term strategic partnership with INL [3]. The fuel fabrication process has been well documented, with appropriate procedures in place to ensure consistent quality, and predictability of the UZr_2 fuel and Zr cladding microstructure. This is important to fuel qualification, and particularly fuel fabrication modeling, as consistency within the fuel and cladding microstructure determines material properties, residual stresses during the fabrication process, and initial geometry and conditions for irradiation.

To support the fabrication process and predict residual stresses and strains, ABAQUS Explicit was utilized to simulate the extrusion process. ABAQUS CAE is a finite element analyses (FEA) code used to solve steady-state or transient thermal-mechanical problems. It does so by allowing the user to import or create geometry within the user interface and mesh the parts appropriately. ABAQUS was chosen over other FEA codes such as ANSYS and DEFORM, due to NQA-1 qualification on the thermal mechanical element being maintained and validated through subsequent releases. ABAQUS CAE has been used to model fuel performance under different programs such as U.S. High Performance Research Reactor Program (HPRR) and PELE, where ANSYS and DEFORM have not [4], [5], [6]. ABAQUS can model the irradiation effects and phenomena of materials by utilizing user defined subroutines, allowing unique material properties to be included in the simulations.

The materials used for the Lightbridge Fuel fabrication activities at INL and in this modeling work are representative of the compositions to be used in Lightbridge's commercial fuel product. The material properties of UZr$_2$ fuel are well characterized within previous work done at INL [7]. Other fuel properties above 600°C that exist within the gamma phase may be extrapolated from work done under the EBR-II and the FFTF MFF programs [8], [9], [10], [11]. The Zr cladding alloy used for the extrusions contains material compositions and properties of typical LWRs [12], [13], [14]. Although it is recognized that the material properties utilized in the modeling efforts are not the exact composition for the materials used within the extrusions and the ABAQUS simulations, they represent the behavior well until material characterization can occur for Lightbridge's specifications.

The ABAQUS simulations presented in this work utilize a direct extrusion process, where the geometry of the tooling and billets was taken from Lightbridge and INL specifications and drawings. Two different extrusion ratios are presented in this work, encompassing a low and high reduction ratio to represent the coextrusion process. Discussion of the model setup using a coupled eulerian lagrangian (CEL) solve is provided, along with the appropriate boundary conditions, thermal and mechanical contact, initial conditions, and predefined fields. Meshing schemes and element types are specified for each instance within the simulations, along with the applicable time scaling schemes utilized to accomplish the simulations in a reasonable amount of computational time. Results for low and high reduction ratio extrusions are presented with resulting stresses, strains, and deformations.

2. METHODOLOGY

All ABAQUS simulations prepared in this work utilize the same material properties from literature [7], [9], [10], [12], [13], [14], [15], [16], [17], [18]. The low and high reduction extrusions share much of the same geometry, with the exception of using different extrusion dies for different reduction ratios. In total, eight different simulations are presented, with each extrusion encompassing different billet lengths, with and without Zr-alloy cladding.

2.1. Extrusion Modeling Geometry Boundary Conditions, and Initial Conditions

During the extrusion process, the cast billet ingots are extruded in order to break up the as-cast microstructure. The reduction ratio from the as-cast ingot to the formed billet assembly is lower than the high reduction ratio used for the coextrusion process. However, these reduction ratios are not final and may be changed depending on the size of the billets and ingot casting molds. For the low reduction extrusions occurring at INL and this modeling effort, the reduction ratios were used to normalize the results obtained with ABAQUS. This ratio is applied to the extrusion die in the modeling efforts. Each simulation included the billet assembly, a copper follower, extrusion die, steel follower block, a steel mechanical ram, bolster, die backer, and a tool steel collet. The relation of this geometry is seen within Figure 1 with named parts in Table I.

Table I. Long Billet with Clad Low Reduction Extrusion Assembly Color Diagram.

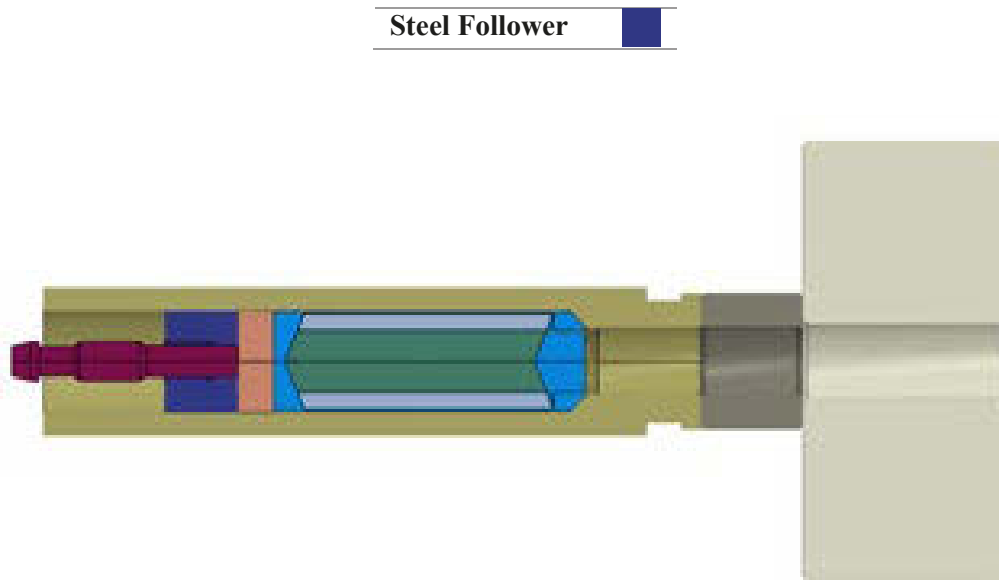| Part	Color
Fuel Billet	
Bolster	
Bronze Canister	
Clad Billet	
Die Backer	
Copper follower	
Primary Die	
Shear Punch	

Figure 1. Long Billet with Clad Low Reduction Extrusion Assembly XZ Plane.

A mechanical stem operating at constant speed is used to push the cast billet and follower through the extrusion die. For the low and high reduction extrusions, this speed is set to a constant. This was accomplished by utilizing a velocity initial condition and boundary condition for the mechanical ram and the steel follower. For both the low and high reduction extrusions, an initial condition of 750°C was applied to the billet material and 450°C to the tooling and dies utilizing a predefined field. The outside lip of the extrusion die and collet are fixed and is accomplished by setting all six degrees of freedom to zero. The die backer and bolster are then tied to the extrusion die and centered along the extrusion axis. In the low reduction extrusions, the extruded material never made contact with the die backer and bolster and thus were removed from the high reduction phase eulerian simulations to further speed up computational efficiency. For mechanical contact, the general ABAQUS contact was deployed, with a friction coefficient of 0.1 specified between the billet material and the tooling.

For the low and high reduction extrusion modeling, thermal mechanical reduced order lagrange elements (C3D8RT) were used for all lagrange part instances with variable element size. The global size specified for these instances was 0.050", with an average aspect ratio of 3.53, and the worst aspect ratio for an element being 6.02 with the shortest edge being 0.0199". For the high reduction phase extrusions, the meshed lagrange billet part instances were used to populate the eulerian mesh utilized for the CEL solve. The eulerian mesh (EC3D8RT) used for the high reduction phase extrusion modeling utilized a more refined mesh to capture the behavior of the extruded bronze, fuel, and cladding. The global size specified for the eulerian mesh was 0.020", with an average aspect ratio of 1.3, and the worst aspect ratio for an element being 2.51 with the shortest edge being 0.00996". The large aspect ratios occur within the extrusion die and the collet to make the mesh the same size as the interfacing eulerian mesh. For FEA, this is more than sufficient for thermal mechanical coupled solves. The Eulerian mesh relationship to the copper follower, extrusion die, and collet for the high reduction phase is shown in Figure 2. The mesh continues along the extrusion axis to accommodate the full length of a billet before flowing through the end of the mesh.
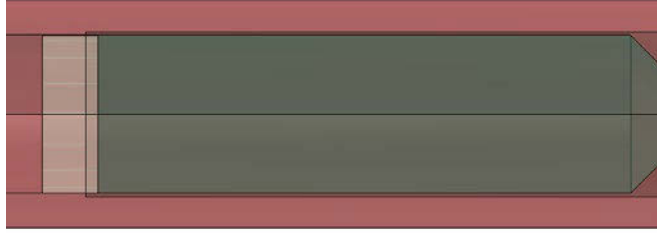
Figure 2. High Reduction Extrusion Assembly Eulerian and Lagrange instance relation.

2.2. Meshing Schemes and Time Scaling

For explicit modeling in ABAQUS, the steady state timestep increment is based on the density of the material, Young's Modulus, and element size. The equation for calculating the stable time increment is below in Equation (1), where L is the element length, E is the Young's Modulus, and p is the material density.

$$\Delta t_{stable} = \frac{L\sqrt{p}}{\sqrt{E}} \tag{1}$$

Due to the element size and the material properties of the extrusion assemblies, the stable time increment is calculated to be ~2.7e-8 seconds. With the number of lagrange and eulerian elements, the computational time to simulate a single billet for the low reduction extrusion is ~1e6 CPU hours and ~8.6e6 CPU hours for the high reduction phase (runtime*CPUs*GHz clock speed). To decrease computational time, ABAQUS offers two different techniques to accelerate simulations. These two techniques include time scaling and mass scaling, although mass scaling is not available for Eulerian elements. To increase the stable timestep increment, artificial time scaling was used. Time scaling is only valid if the energy balance of the simulation remains the same as time and time dependent properties, loads, and boundary conditions scale.

In the case of extrusion modeling, internal energy is converted to plastic dissipation energy by pressing material through the extrusion die. Mass and momentum are conserved through the ABAQUS simulations. Energy is not conserved, as internal energy of the billet is converted to plastic dissipation, with losses coming from friction, heat generation, and hourglass control within elements. The internal energy and the kinetic energy reach a maximum when material flows out of the eulerian mesh, or when all lagrange elements exit the extrusion die for low reduction extrusion simulations. For the energy balance in lagrange and eulerian elements, the sum of plastic dissipation energy and artificial strain energy is equal to internal energy. Although the artificial energy is high (8.47% of internal energy), this was expected due to the high amount of deformation, hour glassing control enabled, and the amount of time scaling (100x) required to execute the solve in a timely manner. As time scaling decreases, so does the internal energy and artificial strain energy of the system. The plastic dissipation energy between the simulations remains the same when normalized.

3. RESULTS: LOW AND HIGH REDUCTION PHASE

The modeling of the low and high reduction extrusions utilized short and long billets, with and without cladding. For the long billet section, the center-to-center length was 1.925", with these dimensions being decreased to 1.250" for the short billet section. Both the short and long billets had enough center-to-center length to see the formation of the "fork" at the front of the billet and the "tail" at the rear of the billets. The remaining material between the tail and fork is considered steady-state, with the stresses and strains not deviating over the length of the steady-state sections. This is shown for the low reduction extrusions and is more evident in the stress and strain states in Figure 3 and Figure 4 below.
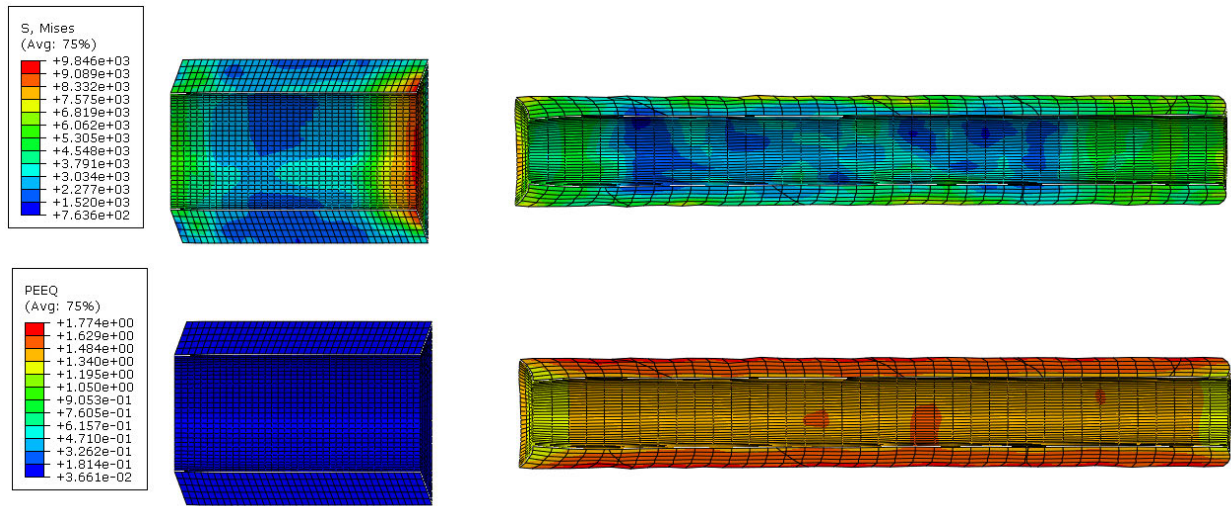
Figure 3. Long Billet with Clad Low Reduction Extrusion Clad Section: Stress (psi, top) and Plastic Strain (bottom). Extruded results enlarged.
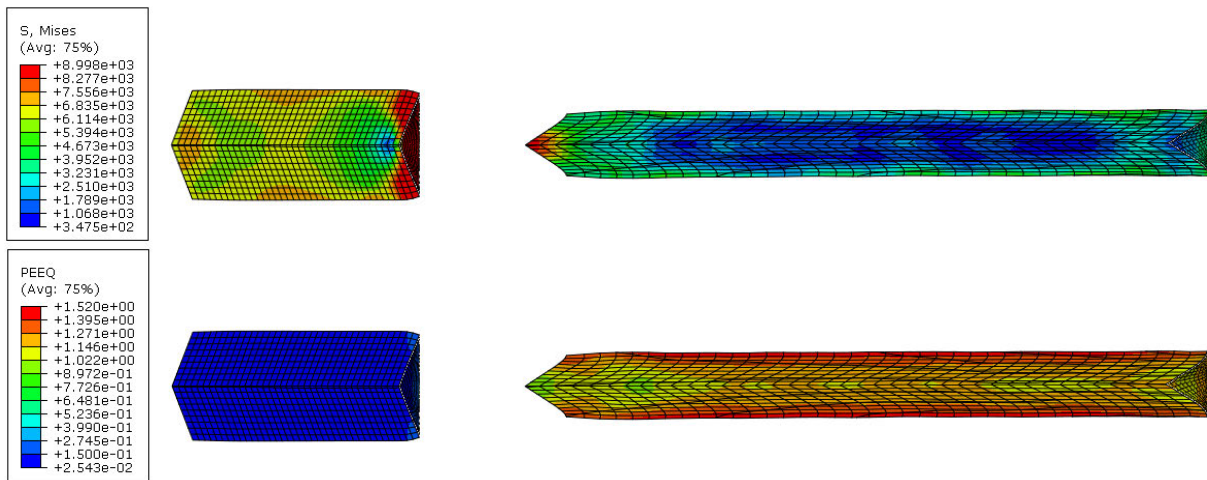

Figure 4. Long Billet with Clad Low Reduction Fuel Section: Stress (psi, top) and Plastic Strain (bottom). Extruded results enlarged.

Table II. Low Reduction Extrusion Simulation Results for key measurements normalized by reduction ratio.

Measurement	Long Billet	Long Billet with Clad	Short Billet	Short Billet with Clad
Fuel Peak Von Mises stress (psi)	8747	8514	8670	8638
Fuel Peak strain	1.793	1.520	1.720	1.509
Clad Peak Von Mises stress (psi)	N/A	10870	N/A	10850
Clad Peak strain	N/A	1.803	N/A	1.790
Fuel OD (in)	0.328"	0.211"	0.326"	0.212"
Clad ID (in)	N/A	0.211"	N/A	0.212"
Clad OD (in)	N/A	0.324"	N/A	0.324"

Bronze thickness (in)	0.007"	0.007"	0.007"	0.007"
Billet OD (in)	0.343"	0.339"	0.341"	0.339"
Fork depth (in)	0.175"	0.136"	0.181"	0.136"
Fork depth with Clad (in)	N/A	0.143"	N/A	0.143"
Tail length (in)	0.130"	0.134"	0.140"	0.136"
Overall extruded length tail end to fork depth (in)	2.019"	2.075"	1.328"	1.326"
Overall extruded length tail end to fork point (in)	2.195"	2.222"	1.476"	1.475"
Extrusion length ratio normalized (Original over Deformed)	1.049	1.078	1.063	1.061

The high reduction phase extrusions utilized the same billet dimensions as the low reduction extrusions, with yield stress occurring sooner in the extrusion die due to the larger reduction ratio. As expected from the high reduction phase extrusion, the depth of the fork is significantly greater than the depth of the low reduction extrusions, but the length of the fork does not scale linearly with the increase of the reduction ratio like the overall length of the billet does. This is shown in Figure 5 and Figure 6. The fork however increases with a ratio of 0.72:1 for both the low and high reduction phase extrusions. It is expected that this ratio is material property, and friction coefficient dependent, as well as the material interactions between the fuel and cladding. This value will be recalculated after a change in material property definitions or geometry occurs.

Due to the high reduction phase extrusions increased reduction ratio over the low reduction extrusions, the stress and plastic deformation within the fuel and cladding is more uniform and significantly higher. The low Von Mises stress seen in the center of the fuel portion of the billet is due to the flow and stress of outer material cancelling out the axial loading force imparted by the copper follower and steel tooling. The cladding does not experience this due to none of the material being on the axial centerline. This same effect occurs between the bronze separators on the extrusion centerline. The steady state sections of the high reduction extrusion phase are shown in Figure 7 and Figure 8. All measurements of the high reduction phase extrusions with cladding material may be found in Table III.
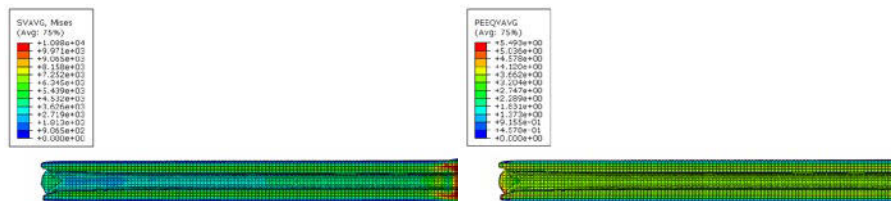

Figure 5. Long Billet with Clad High Reduction Extrusion Clad Section Fork: Stress (psi, left) and Plastic Strain (right)
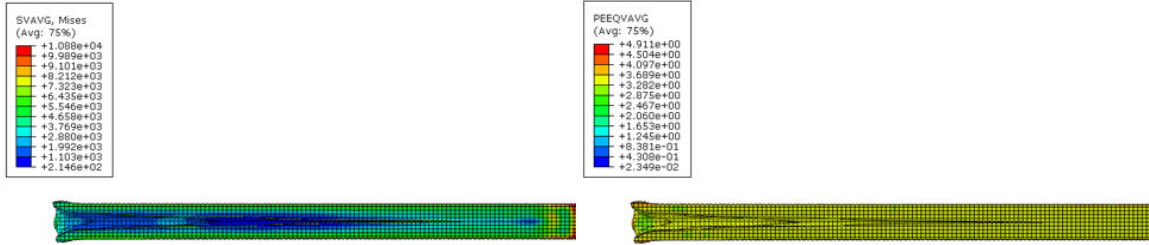
Figure 6. Long Billet with Clad High Reduction Extrusion Fuel Section Fork: Stress (psi, left) and Plastic Strain (right)

When comparing the results within Table II and Table III, the peak fuel stress within each of extrusions reaches the yield stress set within the material models, with slight stress relaxation after the extruded billets are unloaded. Although the extruded billets were not brought to room temperature after the extrusion, the stress states within the billets are expected to increase due to thermal gradients and thermal contraction. Within the fuel billets themselves, the stresses and strains within the center are significantly lower compared to the outer material. This is due to less force needed to deform the material and force it through the extrusion die. The differences within the maximum strains within the cladded and uncladded low reduction extrusions are slight, with the maximum strain occurring within the outmost elements of the extruded material. Looking at differences between the short and long billet extrusions, there is no significant difference in results other than the overall length. Differences between cladded and uncladded extrusions occur within the fork section at the front of each extrusion. In the cladded simulations, the depth of the fork is limited compared to the fuel only. This is due to the cladding having a higher yield stress than the fuel material within the simulations, leading to the element edges deforming less. For the eulerian analysis, the length of the tails and depths of the forks were cut off when their material void fraction dropped below 10%. This was applied to the overall length measurements of the billets as well.
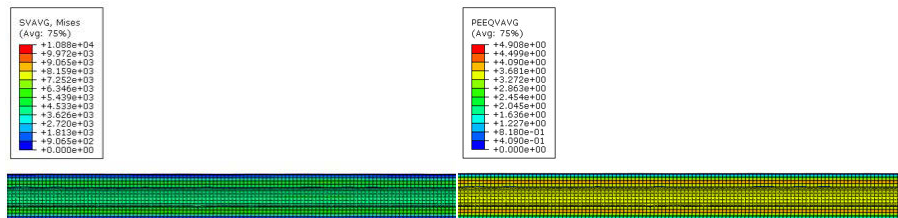

Figure 7. Long Billet with Clad High Reduction Extrusion Clad Steady-State Front Section: Stress (psi, left) and Plastic Strain (right).
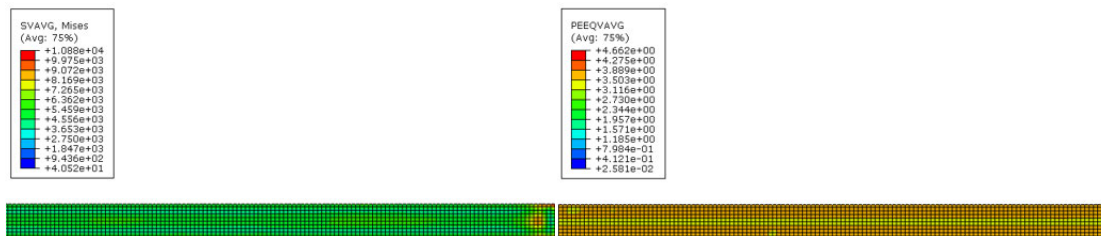

Figure 8. Long Billet with Clad High Reduction Extrusion Fuel Steady-State Front Section: Stress (psi, left) and Plastic Strain (right).

Table III. High Reduction Phase Extrusion Simulation Results for key measurements normalized by reduction ratio.

Measurement	Long Billet	Long Billet with Clad	Short Billet	Short Billet with Clad
Fuel Peak Von Mises stress (psi)	9108	9097	9108	9108
Fuel Peak strain	4.680	3.640	4.807	3.629
Clad Peak Von Mises stress (psi)	N/A	10880	N/A	10880
Clad Peak strain	N/A	4.938	N/A	4.968
Fuel OD (in)	0.011"	0.005"	0.011	0.005"
Clad ID (in)	N/A	0.005"	N/A	0.005"
Clad OD (in)	N/A	0.011"	N/A	0.011"
Billet OD (in)	0.011"	0.011"	0.011"	0.011"
Fork depth (in)	0.139"	0.115"	0.138"	0.119"
Fork depth with Clad (in)	N/A	0.130"	N/A	0.132"
Tail length (in)	0.086"	0.073"	0.091"	0.073"
Overall extruded length tail end to fork depth (in)	1.978"	1.972"	1.243"	1.264"
Overall extruded length tail end to fork point (in)	2.120"	2.103"	1.380"	1.396"
Extrusion length ratio normalized (Original over Deformed)	1.028	1.025	0.994	1.011

The other difference between the low reduction simulations is the reduction ratio that occurs on the billets compared to theoretical values. For the low reduction extrusion simulations, the average normalized reduction ratio calculated out with the deformed meshes was 1.0635. For the high reduction extrusions, the average normalized reduction ratio from deformed meshes was 1.0142. These discrepancies come from the size of the elements chosen for the lagrange and eulerian elements, the hourglass control settings to resolve the plastic distortion, and the material void fraction cutoff. Refinement of the element size would allow for a better estimate of the billet diameter and overall length. Future simulations will include a refined mesh over the extrusion die to better measure the diameter of the fuel and cladding materials. A more accurate overall length measurement of the extrusion may be accomplished by a more refined mesh and a smaller original billet length to save on computational time.

For the high reduction co-extrusions modeled, experimental results from INL have been obtained for the fuel and cladding thicknesses by metallography. The experimental results were normalized by dividing by the produced results within ABAQUS, yielding 1.0006 for the fuel outer diameter and 1.004 for the cladding outer diameter. Further destructive testing and characterization is planned, to include the total lengths of the extruded billets, and the length and depths of the forks and tail. Confirmation of the fuel and cladding outer diameter done at INL facilities gives confidence in the ABAQUS simulations adequately predicting Lightbridge Corporation's fabrication process.

4.   CONCLUSIONS

The preliminary stresses and strains within the low and high reduction extrusions were calculated within ABAQUS Explicit using a combination of lagrange, eulerian, and CEL analysis. The low reduction

extrusions were able to be simulated using lagrange elements, where the high reduction extrusions utilized eulerian elements for the extruded material and lagrange elements for the extrusion tooling for a CEL solve. Both simulation techniques within ABAQUS used time scaling to decrease computational time, and were confirmed to be valid when comparing energy scaling. The low and high reduction extrusions showed that the reduction ratio used on the billets held, as the overall length ratios of the extruded material matched the reduction ratio. The length of the tails and fork depths were smaller for cladded billets in both the low and high reduction extrusions. The low reduction extrusions contained a larger range of stresses and strains throughout the radial sections of the resulted extrusions compared to the high reduction extrusions due to the lower reduction ratio. Although the steady-state extrusion sections of the low and high reduction extrusions allow for insight on the stress and strain states, formation of the fork and tails sections of the extruded material are important for the fuel qualification, specifically length, thickness, and their stress states. The high reduction extrusion ABAQUS results for fuel and cladding outer diameters were compared to INL measurements and were found to be in agreement. This gives confidence that the other length parameters were calculated correctly. The formation of the forks and the tails depend on the friction, the material properties of the extruded material, and the geometry of the billets prior to extrusion.

REFERENCES

[1]   R. Webster, "Fuel Fabrication Development Plan," Reston, Aug. 2020.

[2]   UFuelMet LLC, "Lightbridge Fuel Fabrication Process - Phase 1," Idaho Falls, Jul. 2013.

[3]   Lightbridge Corporation, "Lightbridge Announces Long-Term Strategic Partnership with Idaho National Laboratory," Reston, Dec. 2022.

[4]   H. Ozaltun, M.-H. Herman Shen, P. Medvedev, and S. J. Miller, "Computational evaluation for the mechanical behavior of U10Mo fuel mini plates subject to thermal cycling," *Nuclear Engineering and Design*, vol. 254, pp. 165–178, 2013, doi: 10.1016/j.nucengdes.2012.09.008.

[5]   B. Rabin *et al.*, "Preliminary Report on U-mo Monolithic Fuel for Research Reactors," *Preliminary Report on U-Mo Monolithic Fuel for Research Reactors*, 2017.

[6]   Y.-S. Lee, Y.-J. Choi, S.-J. Kim, Y.-J. Kim, and J.-H. Lee, "A study of the free drop impact characteristics of spent nuclear fuel shipping casks by LS-DYNA3D and ABAQUS," *Journal of the Computational Structural Engineering Institute of Korea*, vol. 18, no. 1, pp. 43–49, 2005.

[7]   G. L. Beausoleil *et al.*, "U-50Zr Microstructure and Property Assessment for LWR Applications," 2021. [Online]. Available: http://www.inl.gov

[8]   C. Matthews, J. Galloway, C. Unal, S. Novascone, and R. Williamson, "BISON for Metallic Fuels Modelling," 2017. [Online]. Available: https://inis.iaea.org/collection/NCLCollectionStore/_Public/49/085/49085900.pdf

[9]   K. M. Paaren, M. D. Gale, P. G. Medvedev, and D. L. Porter, "Fuel performance analysis of Fast Flux Test Facility MFF-3 and -5 fuel pins using BISON with Post Irradiation Examination data," *Nuclear Engineering and Design*, p. 16, 2022.

[10]   K. M. Paaren, M. Gale, M. J. Kerr, P. G. Medvedev, and D. L. Porter, "Initial demonstration of Automated fuel performance modeling with 1,977 EBR-II metallic fuel pins using BISON code with FIPD and IMIS databases," *Nuclear Engineering and Design*, 2021.

[11]   K. M. Paaren *et al.*, "BISON Fuel Performance Modeling Optimization for Experiment X447 and X447A Using Axial Swelling and Cladding Strain Measurements," *Nuclear Engineering and Design*, 2021.

[12]   J. D. Hales *et al.*, "Advanced multiphysics coupling for LWR fuel performance analysis," *Ann Nucl Energy*, 2015, doi: 10.1016/j.anucene.2014.11.003.

[13] R. L. Williamson *et al.*, "Validating the BISON fuel performance code to integral LWR experiments," *Nuclear Engineering and Design*, vol. 301, pp. 232–244, 2016, doi: 10.1016/j.nucengdes.2016.02.020.

[14] K. J. Geelhood, C. E. Beyer, and W. G. Luscher, "PNNL Stress/Strain Correlation for Zircaloy," *PNNL Stress/Strain Correlation for Zircaloy*, 2008.

[15] M. Seif *et al.*, "Temperature-Dependent Material Modeling for Structural Steels: Formulation and Application," Gaithersburg, MD, Apr. 2016. doi: 10.6028/NIST.TN.1907.

[16] J. C. Gentzbittel Rigollet and G. Robert, "High Temperature Mechanical Properties of Unirradiated Dispersion Strengthened Copper."

[17] B. Challa and S. S. Rao, "Study of Mechanical Properties and Microstructural behaviour of alpha-beta brass at elevated temperature," in *E3S Web of Conferences*, EDP Sciences, Oct. 2021. doi: 10.1051/e3sconf/202130901146.

[18] K. M. Paaren, N. Lybeck, K. Mo, P. G. Medvedev, and D. L. Porter, "Cladding Profilometry Analysis of EBR-II metallic fuel pins with HT9, D9, and SS316 cladding," *Energies (Basel)*, 2021.